EPJ manuscript No.
(will be inserted by the editor)

Dynamics of Purcell's three-link microswimmer with a passive elastic tail

Emiliya Passov and Yizhar Or

Faculty of Mechanical Engineering, Technion - Israel Institute of Technology, Israel

the date of receipt and acceptance should be inserted later

Abstract. One of the few possible mechanisms for self-propulsion at low Reynolds number is undulations of a passive elastic tail, as proposed in the classical work of [Purcell, 1977]. This effect is studied here by investigating a variant of Purcell's three link swimmer model where the front joint angle is periodically actuated while the rear joint is driven by a passive torsional spring. The dynamic equations of motion are formulated and explicit expressions for the leading-order solution are derived by using perturbation expansion. The dependence of the motion on the actuation amplitude and frequency is analyzed, and optimization with respect to the swimmer's geometry is conducted.

PACS. 47.63.mf Low Re motion – 87.19.ru Locomotion – 47.10.Fg Dynamical systems methods – 02.30.Mv Approximations and expansions

1 Introduction

The motion of swimming microorganisms is governed by low-Reynolds-number hydrodynamics where viscous drag forces are dominating while inertial effects are negligible [1–3]. In his seminal work, Purcell [4] have coined the famous *scallop theorem*, which states that changing the internal shape of a low-Reynolds-number swimmer in a reciprocal way generates no net motion, due to time-reversibility of the dynamic equations. Purcell proposed a theoretical model of an articulated swimmer composed of three rigid links connected by two rotary joints [Fig. 1] whose angles are changing periodically in a non-reciprocal way which resembles a traveling wave, in order to generate forward motion. Another way which was proposed by Purcell in order to overcome the scallop theorem is waving a flexible tail whose deformation breaks the time-reversibility and thus enables forward motion. Some microorganisms actually adopt these two basic principles for swimming — the nematode *C. Elegans* swims by inducing body undulations that generate a traveling wave [5], and eukaryotic cells such as spermatozoa swim by waving a flexible flagellum which is actuated by molecular motors that generate bending torques [6–9]. Moreover, this mechanism has also been demonstrated experimentally in the artificial microswimmer presented in [10]. Such swimmers are currently the subject of extensive development efforts, mainly for biomedical applications [11].

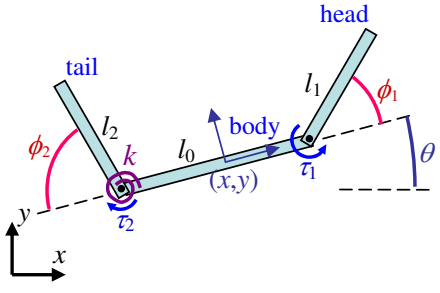

Fig. 1. Purcell's three-link swimmer model.

Many theoretical models of micron-size swimmers have been studied in the literature. One of the earliest works is by G. I. Taylor on the analysis of the "swimming sheet model" representing a flagellated microorganism [12]. Some other classical works on swimming microorganisms are those by Gray and Hancock [13], Lighthill [14] and Blake [15]. More recent works analyzed models of artificial microswimmers whose axisymmetric structure typically induces one-dimensional motion only, e.g. [16–18]. Purcell's three-link swimmer seems to be the simplest model that involves motion of rotation and translation in two dimensions. This model has been revisited in [19], where a detailed analysis was been conducted. The explicit expressions in [19] were derived by assuming slender links and using resistive force theory (RFT) [13, 20]. Optimization of the periodic gait of joint angles has been conducted in [21], and the geometric structure of the dynamic equations has been analyzed in [22]. In contrast to the works mentioned above, which assume that the kinematics of joint angles are directly prescribed, the recent work [23] studies the dynamics of Purcell's three-link swimmer under actuation of the *torques* at the two joints in a prescribed time-periodic profile, and analyzes the dynamic stability of the resulting shape kinematics. The goal of the present work is to study the dynamics of the three-link swimmer where one rotary

joint is periodically actuated while the other joint is passively acted by a torsional spring which represents an elastic tail. This simplified model enables explicit analysis of the resulting dynamics of the swimmer's discrete degrees-of-freedom, and avoids the complication associated with models of continuous elastic filaments whose motion is governed by partial differential equations as in [24–26]. Thus, it serves as a minimalistic representative model of a microswimmer that locomotes by applying local actuation and exploiting structural flexibility in order to propagate body undulations. The next section presents the problem, describes the swimmer's model, and formulates its governing equations of motion. Section 3 derives leading-order expressions of the swimmer's motion and energy expenditure by applying small-amplitude perturbation expansion. Finally, Section 4 studies optimization of swimming in terms of the actuation frequency and the swimmer's geometric structure, under different performance measures.

2 Problem Formulation

We begin by describing Purcell's three-link swimmer model and formulating the dynamic equations which govern its motion. The swimmer, depicted in Fig. 1, consists of three elongated rigid links whose lengths are l_0, l_1 and l_2, which are connected by two rotary joints. The swimmer's motion is assumed to be confined to the xy plane. The shape of the swimmer is described by the two relative angles between the links, denoted by $\mathbf{\Phi} = (\phi_1, \phi_2)^T$. The location of the swimmer is described by the planar position and orientation of a reference frame which is attached to the central link, and is denoted by $\mathbf{q} = (x, y, \theta)^T$. The two internal torques acting at the rotary joints [Fig. 1] are denoted by τ_1 and τ_2 and by the vector $\boldsymbol{\tau} = (\tau_1, \tau_2)^T$. The controlled input of the swimmer is the "head angle" ϕ_1, which is given a harmonic excitation $\phi_1(t) = \varepsilon \sin(\omega t)$. A passive torsional spring is attached to the second joint, such that the internal torque is proportional to the tail angle ϕ_2 and satisfies $\tau_2 = -k\phi_2$, where k is the elasticity constant. The actuated link of length l_1 represents the swimmer's head, the passive link of length l_2 represents the swimmer's tail, and the central link of length l_0 represents the swimmer's body. Finally, the swimmer is submerged in an unbounded domain of viscous fluid whose motion is governed by Stokes equations [2].

We now formulate the dynamics of the swimmer, which is based on two fundamental differential equations. The first equation relates the velocity of the shape variables $\dot{\mathbf{\Phi}}$ to the swimmer's body velocity $\dot{\mathbf{q}}$ as

$$\dot{\mathbf{q}} = \mathbf{D}(\theta)\mathbf{G}(\mathbf{\Phi})\dot{\mathbf{\Phi}}, \text{ where } \mathbf{D}(\theta) = \begin{pmatrix} \cos\theta & -\sin\theta & 0 \\ \sin\theta & \cos\theta & 0 \\ 0 & 0 & 1 \end{pmatrix}. \quad (1)$$

Note the special structure of (1), which is due to the fact that the body velocity $\dot{\mathbf{q}}$ expressed in body-fixed reference frame depends only on the shape variables $\mathbf{\Phi}$ and their velocity $\dot{\mathbf{\Phi}}$. This property is called *gauge symmetry* [27], and stems from the lack of external boundary conditions in unbounded fluid domains. The second equation relates the velocity of the shape variables to the internal torques acting at the joints, as

$$\dot{\mathbf{\Phi}} = \mathbf{H}(\mathbf{\Phi})\boldsymbol{\tau}. \quad (2)$$

The detailed derivation of these two equations appears in the supplementary document [33]. It is based on the fact that for rigid bodies in Stokes flow, forces and velocities are linearly related by a resistance tensor [2], and that the motion is quasi-steady, so that each rigid body is in static equilibrium at all times. The equations of motion in (1) and (2) are then formulated in [33] in terms of the (unknown) resistance tensor, and it is shown that the matrix $\mathbf{H}(\mathbf{\Phi})$ in (2) is symmetric and positive definite. Furthermore, explicit expressions for $\mathbf{G}(\mathbf{\Phi})$ and $\mathbf{H}(\mathbf{\Phi})$ are derived in [33] by utilizing *resistive force theory* (RFT) [13,20]. Under this simplifying theory, the force and torque exerted by the fluid at each point on the boundary of a slender body depend only on the local velocity of this point, and any interaction with the motion of other neighboring points is neglected. While all the numerical simulations in this paper are based on RFT formulation, the analysis presented here is completely general, and is not limited to this specific choice of hydrodynamic resistance formulation.

In order to formulate the governing dynamic equation for the swimmer with a passive elastic tail, further manipulation of (1) and (2) is needed, as follows. Inverting (2), one obtains $\tau_2 = (-H_{21}(\mathbf{\Phi})\dot{\phi}_1 + H_{11}(\mathbf{\Phi})\dot{\phi}_2)/\Delta(\mathbf{\Phi})$, where $\Delta(\mathbf{\Phi}) = \det(\mathbf{H}(\mathbf{\Phi})) = H_{11}H_{22} - H_{21}H_{12}$ and H_{ij} is the (i,j)-element of $\mathbf{H}(\mathbf{\Phi})$. Substitution of the elasticity relation $\tau_2 = -k\phi_2$ then gives

$$\dot{\phi}_2 = -kN(\mathbf{\Phi})\phi_2 - F(\mathbf{\Phi})\dot{\phi}_1, \quad (3)$$

where $N(\mathbf{\Phi}) = \Delta(\mathbf{\Phi})/H_{11}(\mathbf{\Phi})$ and $F(\mathbf{\Phi}) = -H_{21}(\mathbf{\Phi})/H_{11}(\mathbf{\Phi})$. Since the head angle is given as $\phi_1(t) = \varepsilon\sin(\omega t)$, Eq. (3) is a nonlinear first-order differential equation in ϕ_2 with time-periodic excitation, which governs the dynamics of the flexible tail and, in turn, dictates the net body motion of the swimmer via Eq. (1). An important observation is that the presence of elasticity introduces a *characteristic time scale* of the swimmer. This characteristic time can be interpreted as the "response time" of the spring, and is defined as follows. Let l_c denote a characteristic length scale of the swimmer, so that the link lengths l_0, l_1 and l_2 are all of order $O(l_c)$. If v_c is a characteristic swimming velocity of the swimmer, then drag forces scale as $\mu l_c v_c$, where μ is the fluid viscosity. The torsional spring constant k has torque units and scales as $\mu l_c^2 v_c$. Thus, a characteristic time t_c of this swimmer scales as $t_c \sim \mu l_c^3/k$, where a particular value for t_c is chosen in the next section. The existence of this time scale is a fundamental difference of this elastic swimmer from previous models of Purcell's swimmer where the controlled input was either the joint angles $\mathbf{\Phi}(t)$ as in [19,21] or the internal torques $\boldsymbol{\tau}(t)$ as in [23]. In these cases, the dynamics is time-independent and scaling the time by $t \to \alpha t$, the angles by $\mathbf{\Phi}(t) \to \mathbf{\Phi}(\alpha t)$ and the torques by $\boldsymbol{\tau} \to \alpha\boldsymbol{\tau}(\alpha t)$ leaves the swimmer's motion invariant. Here, actuation of the head angle $\phi_1(t)$

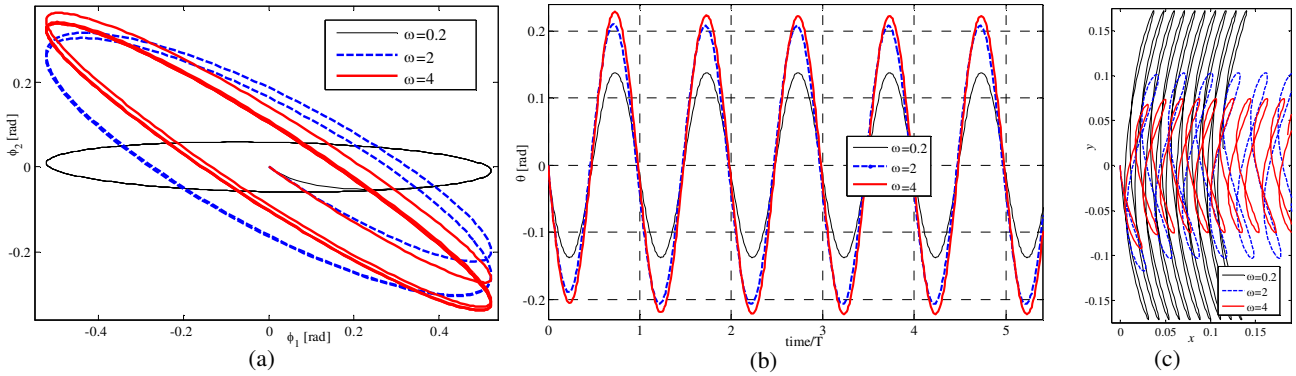

Fig. 2. Simulation results for three actuation frequencies — (a) Trajectories in (ϕ_1, ϕ_2)-plane. (b) Body orientation θ vs. time. (c) Trajectory of body's center in (x, y)-plane.

with different frequencies ω results in significantly different motion, as demonstrated in the following example.

Simulation example: In order to illustrate the dynamic behavior of the system, we simulate the motion of the swimmer with identical links having lengths $l_0 = l_1 = l_2 = 1$ and radius of $a = 0.1$, using RFT formulation of the hydrodynamics (see [33] for details). Time is scaled such that $\mu l_c^3/k = 1$. The actuation amplitude is $\varepsilon = \pi/6$ and three different actuation frequencies $\omega = \{0.2, 2, 4\}$ are chosen. The tail angle $\phi_2(t)$ and swimmer's location $\mathbf{q}(t)$ are obtained by numerically integrating (3) and (1), under initial conditions $\phi_2(0) = 0$ and $\mathbf{q}(0) = (0, 0, 0)^T$. Simulations were conducted by using the procedure `ode45` in MATLAB, which implements a Runge-Kutta integration scheme with an adaptive step size. Fig. 2(a) shows the resulting trajectories of the joint angles in (ϕ_1, ϕ_2)-plane. It can be seen that the trajectories rapidly converge to a closed loop which represents a periodic solution of $\phi_2(t)$ in coordination with the imposed actuation of $\phi_1(t)$. Fig. 2(b) plots the swimmer's orientation $\theta(t)$ as a function of time normalized by the actuation period $T = 2\pi/\omega$, showing that it also converges to a time-periodic function. This indicates that on average, the swimmer moves along a straight line without net rotation. Fig. 2(c) plots the trajectory of the swimmer's body frame $x(t), y(t)$ in xy plane. One can see that the net motion is almost exactly along the x axis, directed towards the head (link 1), and that the linear distance traveled in one period i.e. $t = T$ is approximately $\{0.012, 0.03, 0.019\}$ for $\omega = \{0.2, 2, 4\}$, respectively. This indicates that when the actuation frequency ω is too low or too high, the net forward motion of the swimmer per period is small compared to intermediate frequencies. A natural question to ask is whether there exists an optimal frequency which produces the maximal net forward motion. This question is addressed in Section 4 after derivation of asymptotic expressions for the swimmer's motion in the next section.

3 Asymptotic Analysis

In this section, the dynamics of the swimmer is analyzed by using perturbation expansion [28] of equations (3) and (1) assuming small actuation amplitude ε, and asymptotic expressions involving leading-order terms in ε are formulated. The solution of (3) is expressed as a power series $\phi_2(t) = \varepsilon f_1(t) + \varepsilon^2 f_2(t) + \varepsilon^3 f_3(t) + \cdots$, and is then solved for $f_i(t)$ for leading orders of ε by expanding the right hand side of (3) as a Taylor series about $\phi_1 = \phi_2 = 0$. Initial conditions $\phi_2(0) = 0$ and $\mathbf{q}(0) = (0, 0, 0)^T$ are assumed. The first-order terms of (3) give rise to the linear differential equation given by

$$\dot{f}_1 = -kN_0 f_1 - \omega F_0 \cos(\omega t), \tag{4}$$

where $N_0 = N(\mathbf{\Phi} = 0)$ and $F_0 = F(\mathbf{\Phi} = 0)$. Using the RFT formulation (see [33] for details), these expression are explicitly given by

$$\begin{aligned} N_0 &= \frac{3\ln(l_c/a)}{4\pi\mu} \cdot \frac{(l_0+l_1+l_2)^3}{l_2^3(l_0+l_1)^3} > 0 \\ F_0 &= \frac{l_1^2(3l_0l_1+3l_0l_2+2l_1l_2+3l_0^2)}{2l_2(l_0+l_1)^3} > 0 \end{aligned} \tag{5}$$

From equation (4), we choose the characteristic frequency and time scale as $\omega_c = kN_0$, and $t_c = 1/\omega_c$. The solution of (4) is then given by

$$\begin{aligned} &f_1(t) = B(\omega)\,(e^{-\omega_c t} - \cos(\omega t)) - A(\omega)\sin(\omega t), \\ &\text{where } A(\omega) = \frac{\omega^2 F_0}{\omega^2 + w_c^2} \text{ and } B(\omega) = \frac{\omega_c \omega F_0}{\omega^2 + w_c^2}. \end{aligned} \tag{6}$$

It is readily seen that the leading-order $O(\varepsilon)$ solution of $\phi_2(t)$ given in (6) has a component of transient response which decays exponentially, and a harmonic steady-state response with the actuation frequency ω, whose amplitude and phase shift depend on ω. Due to symmetry of the swimmer about the axis of the middle link — *axisymmetry*, it can be verified that both $N(\mathbf{\Phi})$ and $F(\mathbf{\Phi})$ in (3) are even functions in $\mathbf{\Phi}$, i.e. $N(\mathbf{\Phi}) = N(-\mathbf{\Phi})$, $F(\mathbf{\Phi}) = F(-\mathbf{\Phi})$. This implies that the ε^2-term of ϕ_2 satisfies the equation $\dot{f}_2 = -kN_0 f_2$. Therefore, $f_2(t)$ decays to zero as fast as $e^{-\omega_c t}$, and one concludes that at a steady state, the first-order solution of $\phi_2(t)$ given in (6) is accurate even up to order $O(\varepsilon^2)$.

Next, we compute the leading-order solution of the swimmer's body motion $\mathbf{q}(t)$ from Eq. (1), by denoting $x(t)=\varepsilon g_1^x(t)+\varepsilon^2 g_2^x(t)+\cdots$, $y(t)=\varepsilon g_1^y(t)+\varepsilon^2 g_2^y(t)+\cdots$, and $\theta(t)=\varepsilon g_1^\theta(t)+\varepsilon^2 g_2^\theta(t)+\cdots$. From the structure of (1), the equation for $\theta(t)$ is independent of θ, and is given by $\dot\theta = G_{31}(\mathbf{\Phi})\dot\phi_1 + G_{32}(\mathbf{\Phi})\dot\phi_2$, where $G_{ij}(\mathbf{\Phi})$ is the (i,j)-element of $\mathbf{G}(\mathbf{\Phi})$ in (1). The first-order term of $\theta(t)$ then satisfies

$$\dot g_1^\theta(t) = Q_1\omega\cos(\omega t) + Q_2\dot f_1(t), \tag{7}$$

where $Q_1 = G_{31}(\mathbf{\Phi}=0)$ and $Q_2 = G_{32}(\mathbf{\Phi}=0)$. The explicit expressions for Q_1 and Q_2 under the RFT formulation are given in [33]. The first-order solution for $\theta(t)$ is then given by

$$g_1^\theta(t) = (Q_1 - A(\omega)Q_2)\sin(\omega t) + B(\omega)Q_2(e^{-\omega_c t}-\cos(\omega t)). \tag{8}$$

It can be seen that at steady state, the leading order solution of $\theta(t)$ is harmonic oscillations with ω-dependent amplitude and phase shift.

In order to derive leading-order expressions of the swimmer's linear motion $x(t)$ and $y(t)$, one has to expand the (x,y)-components of the right hand side of Eq. (1) as a multivariable Taylor series in ϕ_1, ϕ_2 and θ about $\phi_1=\phi_2=\theta=0$. Importantly, due to the swimmer's axisymmetry, elements of the first row of $\mathbf{G}(\mathbf{\Phi})$ are odd functions of $\mathbf{\Phi}$, i.e. $G_{1j}(-\mathbf{\Phi}) = -G_{1j}(\mathbf{\Phi})$ for $j=1,2$, while elements of the second row of $\mathbf{G}(\mathbf{\Phi})$ are even functions of $\mathbf{\Phi}$, i.e. $G_{2j}(-\mathbf{\Phi}) = G_{2j}(\mathbf{\Phi})$. This implies some simplification of the expansion, as well as significant differentiation between the behavior of leading order solutions of x and y. The first-order terms in the equations for $x(t)$ and $y(t)$ are given as

$$\dot g_1^x(t) = 0, \quad \dot g_1^y(t) = Z_1\omega\cos(\omega t) + Z_2\dot f_1(t), \tag{9}$$

and the second-order terms are given as

$$\begin{aligned}\dot g_2^x(t) &= (P_{11}\sin(\omega t) + P_{12}f_1(t))\,\omega\cos(\omega t)\\ &\quad + (P_{21}\sin(\omega t) + P_{22}f_1(t))\,\dot f_1(t)\\ &\quad - g_1^\theta(t)\left(Z_1\omega\cos(\omega t) + Z_2\dot f_1(t)\right),\\ \dot g_2^y(t) &= 0\end{aligned} \tag{10}$$

where $Z_j = G_{2j}(\mathbf{\Phi}=0)$ and $P_{jk} = \left.\dfrac{\partial G_{1j}}{\partial\phi_k}\right|_{\mathbf{\Phi}=0}$ for $j,k=1,2$. The explicit expressions for Z_j and P_{jk} under RFT formulation are given in [33]. It can be seen that $x(t)$ is only of order ε^2 while $y(t)$ is of order ε. Due to the swimmer's axisymmetry, it can be verified that the next order of nonzero term is ε^4 for x and ε^3 for y. The first-order solution for $y(t)$ is given by

$$g_1^y(t) = (Z_1 - A(\omega)Z_2)\sin(\omega t) + B(\omega)Z_2(e^{-\omega_c t}-\cos(\omega t)). \tag{11}$$

Thus, to leading order, $y(t)$ has a decaying transient term and a steady-state term of a harmonic function with zero mean. Thus, the net motion in y direction per period is zero to leading order, and grows only as $O(\varepsilon^3)$. The second-order solution for $x(t)$ at steady state (i.e. after omission of the decaying exponents for brevity) is given by

$$g_2^x(t) = C(\omega)\sin(2\omega t) + D(\omega)(1-\cos(2\omega t)) + B(\omega)E\omega t,$$

where

$$\begin{aligned}C(\omega) &= \tfrac{1}{4}B(\omega)\left(Q_1Z_2 + Q_2Z_1 - P_{12} - P_{21} - 2A(\omega)(Q_2Z_2 - P_{22})\right)\\ D(\omega) &= \tfrac{1}{4}\left(P_{11} - Q_1Z_1 + (Q_2Z_1 + Q_1Z_2 - P_{12} - P_{21})A(\omega)\right.\\ &\quad \left. + (P_{22} - Q_2Z_2)(A(\omega)^2 - B(\omega)^2)\right)\\ E &= \tfrac{1}{2}(P_{21} - P_{12} + Q_2Z_1 - Q_1Z_2)\end{aligned} \tag{12}$$

Thus, to leading order, $x(t)$ is a superposition of zero-mean harmonic oscillations with a constant-rate expression, which is precisely the net forward motion of the swimmer. The net forward progress of the swimmer in a complete period, i.e. $t\in[0,2\pi/\omega]$ is thus given by

$$X = 2\pi\varepsilon^2 B(\omega)E + O(\varepsilon^4). \tag{13}$$

The *average swimming speed* is defined as $\overline{V} = \frac{\omega}{2\pi}X$, and its leading-order expression is given by

$$\overline{V} = \varepsilon^2 B(\omega)E\omega + O(\varepsilon^4). \tag{14}$$

We now compute the leading order expression of the swimmer's mechanical power expenditure. The instantaneous power (i.e. rate of mechanical work) injected into the system is simply the work rate of the actuated joint, given by $P(t) = \tau_1(t)\dot\phi_1(t)$. Using (2) one obtains $\tau_1 = (H_{22}\dot\phi_1 - H_{12}\dot\phi_2)/\Delta$. Using the leading-order expression for ϕ_2 in (6), one obtains the leading order expression for the power $P(t)$ at steady state as

$$\begin{aligned}P(t) = \varepsilon^2\omega^2\,&[-J_1(A(\omega)\cos(\omega t) - B(\omega)\sin(\omega t))\\ &+ J_2\cos(\omega t)]\cos(\omega t) + O(\varepsilon^4)\end{aligned} \tag{15}$$

where $J_1 = -H_{12}(0)/\Delta(0)$ and $J_2 = H_{22}(0)/\Delta(0)$. The mechanical work per period is then given by

$$W = \int_0^{2\pi/\omega} P(t)dt = \pi\varepsilon^2\omega(J_2 - A(\omega)J_1) + O(\varepsilon^4). \tag{16}$$

Using the definitions of J_1, J_2 and $A(\omega)$ and the fact that $\mathbf{H}(\mathbf{\Phi})$ is symmetric and positive-definite, it can be easily proven that $J_2 - A(\omega)J_1 > 0$ for all ω, so that the work W is always positive. The time-averaged power expenditure is given by

$$\overline{P} = \frac{\omega}{2\pi}W = \varepsilon^2\omega^2(J_2 - A(\omega)J_1)/2 + O(\varepsilon^4). \tag{17}$$

In order to verify the theoretical results, we compare them with numerical simulations. Fig. 3(a) shows the steady-state trajectories of the joint angles in (ϕ_1,ϕ_2)-plane for $\omega=\omega_c$ and different actuation amplitudes ε. The dashed curves are computed based on the leading-order analytic expression derived in (6), while the solid curves are obtained by numerical integration of (3) and (1). It can be seen that the $O(\varepsilon^3)$ deviation between the numerical and

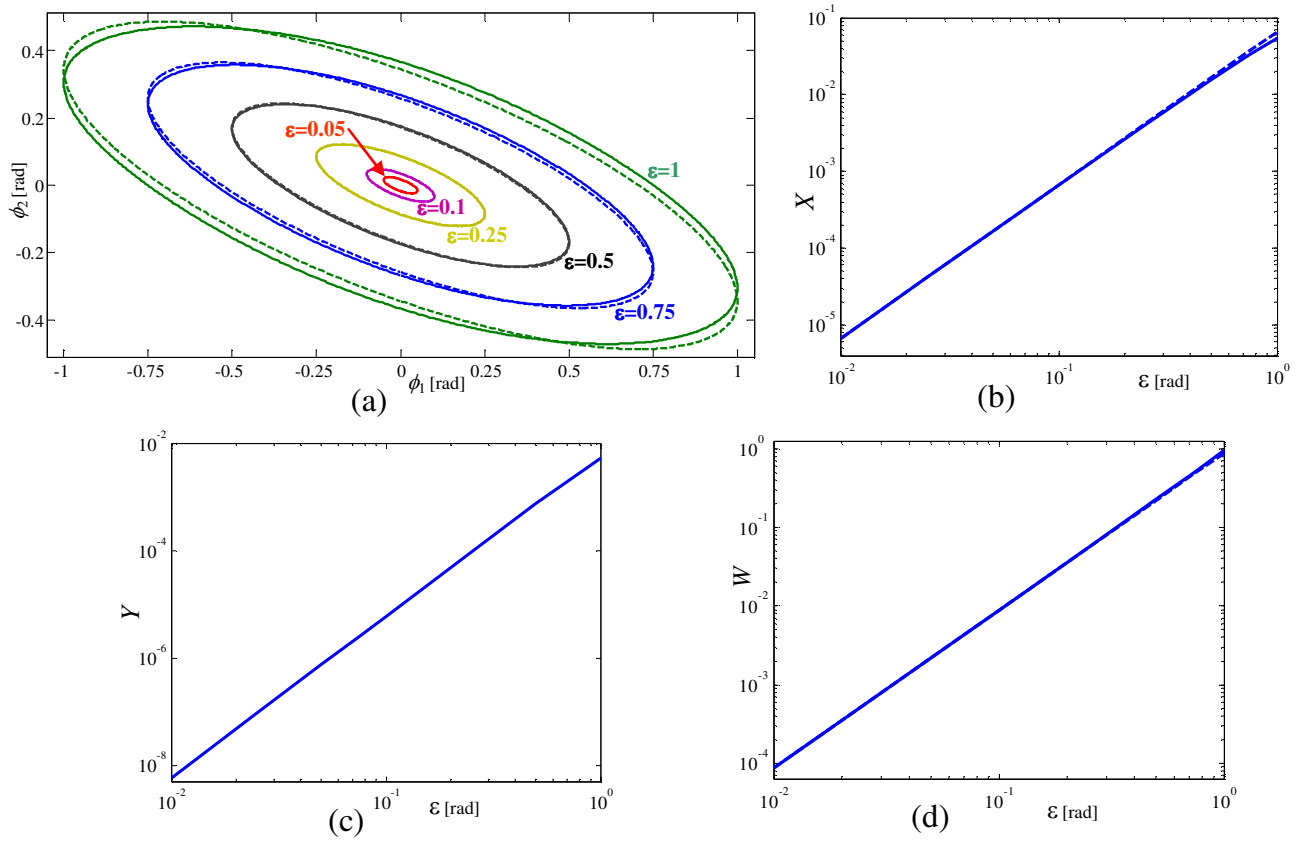

Fig. 3. Comparison of numerical simulations with leading-order predictions at $\omega = \omega_c$ — (a) Trajectories in (ϕ_1, ϕ_2)-plane for different actuation amplitudes ε. (b) Net motion in x direction vs. ε. (c) Net motion in y direction vs. ε. (d) Mechanical work per period W vs. ε.

analytical curves becomes visible only for large values of ε. Figures 3(b),(c) and (d) show plots of the net motion in x direction, the net motion in y direction, and the mechanical work W, respectively, in a single period as a function of the amplitude ε for actuation frequency $\omega = \omega_c$. The plots appear on log-log axes in order to better visualize the power-law dependencies on ε, and compare between the analytic expressions (dashed curves) and the numerical simulation results (solid curves). It can be seen that to leading order, X and W are indeed of $O(\varepsilon^2)$, and that the net motion in y direction is $O(\varepsilon^3)$, as predicted. Note that the reason for the high accuracy of the analytical leading-order expressions is that the error terms are two orders higher. This is due to the functions $N(\mathbf{\Phi})$ and $F(\mathbf{\Phi})$ in (3) being even in $\mathbf{\Phi}$, which is a consequence of the swimmer's symmetry about its longitudinal axis.

4 Optimality considerations

In this section we use the asymptotic results in order to study various optimality criteria for the swimmer model. We first seek for the optimal actuation frequency, and then seek for the optimal geometric structure of the swimmer. Naturally, in both cases optimality depends crucially on the choice of the performance measure that one wishes to optimize. In the following, we study four different performance measures which lead to four different interpretations of optimality.

4.1 Optimal actuation frequency

We begin by studying the influence of the actuation frequency ω on the swimming performance measures. As explained above, the existence of a time scale induced by the elasticity constant k implies that the swimmer's behavior strongly depends on ω, in contrast to "kinematic swimmers" where the prescribed input is the shape change (e.g. $\mathbf{\Phi}(t)$ as in [19,21]), for which the dynamic equations are time-invariant.

The first performance measure is the net forward motion per period X, whose leading order expression was formulated in (13). Interestingly, it can be shown that for very slow actuation $\omega \to 0$, X scales like ω, and that for very fast actuation $\omega \to \infty$, X scales like $1/\omega$, so that in both cases the net motion X vanishes. The physical explanation is that in the limit of $\omega \to 0$ the torsional spring responds immediately, so that the second joint can be regarded as perfectly rigid, fixed at $\phi_2 = 0$, whereas in the limit of $\omega \to \infty$, the spring is too slow to respond, so the joint can be regarded as free, i.e. $\tau_2 = 0$. In both cases, the swimmer performs a perfectly reciprocal motion

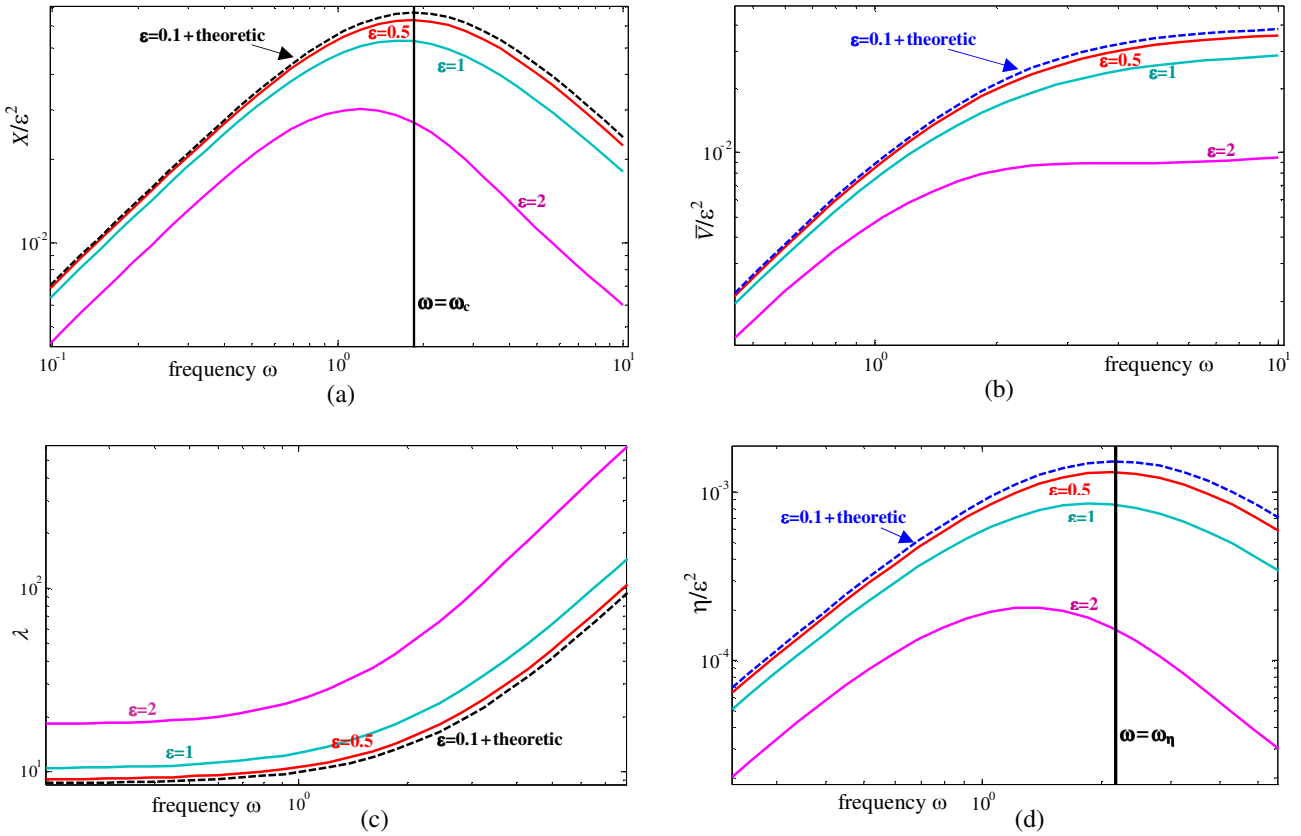

Fig. 4. Comparison of analytical expressions (dashed) and simulation results (solid) as a function of actuation frequency ω — (a) Scaled forward motion per period X/ε^2. (b) Scaled average forward velocity $\overline{V}/\varepsilon^2$. (c) Average mechanical work per travel distance $\lambda = W/X$. (d) Scaled Lighthill's efficiency η/ε^2.

which, according to the scallop theorem [4], gives zero net motion. In the range of intermediate actuation frequencies, it can be easily verified that to leading order, the frequency ω which maximizes X is precisely the characteristic frequency $\omega_c = kN_0$, and that the corresponding maximal distance is given by $X^* = \pi\varepsilon^2 F_0 E$.

The second performance measure is the average swimming velocity $\overline{V}$. The leading-order expression in (14) indicates that $\overline{V}$ increases monotonically with ω, yet it converges to a finite upper bound of $V^* = \varepsilon^2\omega_c F_0 E$ for $\omega \to \infty$. It is important to note that this result, which is based on the assumption of quasistatic motion, is not necessarily valid at very high actuation frequencies $\omega \to \infty$. This is because at large *Strouhal number*, defined as $St = \omega l_c / v_c$, inertial effects due to motion of the swimmer's links are no longer negligible. Moreover, at this limit of $\omega \to \infty$ the expression for the required energy expenditure grows unbounded, as discussed next.

The third performance measure is the *mechanical work per travel distance*, denoted by λ. Using the expressions in (13) and (16), λ is given by

$$\lambda = \frac{W}{X} = \frac{(J_2 - F_0 J_1)\omega^2 + J_2\omega_c^2}{2\omega_c F_0 E} + O(\varepsilon^2). \qquad (18)$$

Equation (18) indicates that λ is minimized when the actuation frequency is as low as possible ($\omega \to 0$) where both W and X vanish, and its minimal value is given by $\lambda^* = \dfrac{J_2\omega_c}{2F_0 E}$. Interestingly, this finding is again in contrast to "kinematic swimmers", for which the quantity W/X can be made arbitrarily small by choosing the actuation as slow as possible since X is a purely geometric quantity, independent of time scaling. This time invariance is the reason why *Lighthill's efficiency* was commonly chosen as a measure of energetic efficiency for optimization of microswimmers, as discussed next.

The fourth performance measure is Lighthill's efficiency, denoted by η. It was originally defined as the mechanical power required to drag the swimmer at a given velocity by an externally applied force, divided by the actual power required for swimming at the same velocity, cf. [29,30]. For swimmers which change their shape periodically the definition is slightly adapted – the dragging power is taken for a swimmer whose shape is fixed at some reference configuration, while the swimming power and swimming velocity are taken in an averaged sense, i.e. $\overline{P} = W/T$ and $\overline{V} = X/T$ where T is the period of the stroke, cf. [31,21,32]. For a given swimmer, it is readily shown that η is proportional to $\overline{V}^2/\overline{P}$. Using equations (14) and (17) and ignoring the proportionality factor, one obtains

$$\eta = \frac{\overline{V}^2}{\overline{P}} = \frac{2\varepsilon^2\omega^2(\omega_c F_0 E)^2}{J_2(\omega^2+\omega_c^2)^2 - J_1\omega^2 F_0(\omega^2+\omega_c^2)} + O(\varepsilon^4). \qquad (19)$$

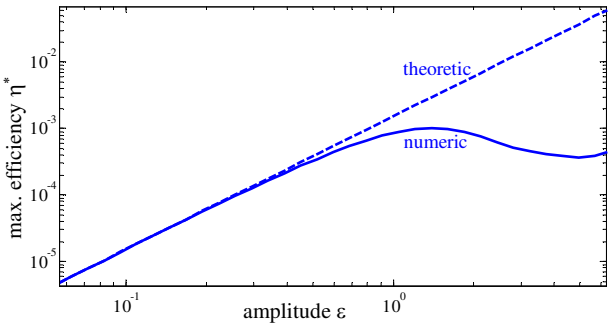

Fig. 5. The optimal Lighthill's efficiency η^* as a function of actuation amplitude ε — numerical (solid) and theoretical (dahsed).

For fixed actuation amplitude ε, using elementary calculus one obtains that η is maximized at a frequency ω_η which is given by

$$\omega_\eta = \left(\frac{J_2}{J_2 - J_1 F_0}\right)^{1/4} \omega_c = \left(\frac{H_{11}(0)H_{22}(0)}{\Delta(0)}\right)^{1/4} \omega_c. \tag{20}$$

Using the fact that $\mathbf{H}(\mathbf{\Phi})$ is symmetric and positive-definite, it can be shown that $\omega_\eta > \omega_c$.

Next, we present results of numerical simulations which validate the theoretical predictions regarding the dependence of the four performance measures on the actuation frequency ω. Figures 4(a),(b),(c) and (d) show log-log plots of the scaled net distance X/ε^2, the scaled average velocity $\overline{V}/\varepsilon^2$, the energy per distance λ, and the scaled Lighthill efficiency η/ε^2 respectively, as a function of the frequency ω for different actuation amplitudes ε. It can be seen that the differences between the analytic expressions (dashed curve) and the numerical results (solid curves) become more evident as ε is increased. In particular, Fig. 4(a) shows that for larger amplitudes ε, the maximal forward distance X is attained at an optimal frequency which is smaller than ω_c. Similarly, Fig. 4(d) shows that the maximal Lighthill efficiency η^* is attained at an optimal frequency which is smaller than ω_η. The reason for this bias is the contribution of higher-order terms in ε.

The fact that the leading-order expression for η in (19) is proportional to ε^2 indicates that strokes with small actuation amplitude ε are inefficient. On the other hand, it does not imply that the Lighthill efficiency grows monotonically with ε for large amplitudes. As an example, Fig. 5 plots the value of the optimal efficiency η^* as a function of ε in log-log axes. The solid curve is the optimal efficiency η^* computed numerically by discretizing the set of frequencies ω and estimating the frequency which maximizes η for each amplitude ε. The dashed line is the leading order expression for the maximal efficiency obtained by substituting $\omega = \omega_\eta$ from (20) into (19) in order to obtain $\eta(\omega_\eta)$, yielding an expression which is simply quadratic in ε. One can see that the optimal efficiency η^* is *non-monotonic* in ε, and that its global maximum is attained at $\varepsilon \approx 1.4 = 80°$. Clearly, this effect cannot be captured by the leading-order analysis conducted in this work, as it is also due to the influence of higher-order terms in ε.

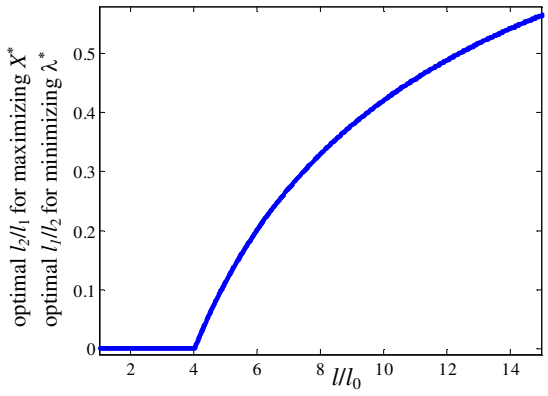

Fig. 6. The optimal ratio l_2/l_1 for maximizing X^*, which is equal to the optimal ratio l_1/l_2 for minimizing λ^*, as a function of the total length l.

4.2 Optimal swimmer

Next, we study optimization of the swimmer's geometric structure, either for maximizing the net forward motion per period X, or for minimizing the work per travel distance λ. We focus on the maximal distance X^* which is attained at $\omega = \omega_c$ and the minimal value λ^* which is attained at $\omega \to 0$. Using RFT formulation, explicit expressions are obtained for these quantities in terms of the links' lengths, as follows:

$$X^* = \pi l_0 l_1^3 \frac{(3l_1l_0 + 3l_2l_0 + 2l_1l_2 + 3l_0^2)(l_1^2 + l_1l_2 + l_1l_0 + l_2^2 + l_2l_0)}{8(l_1 + l_0)^3(l_1 + l_2 + l_0)^4}$$
$$\lambda^* = 2k \frac{(l_2 + l_0)^3(l_1 + l_2 + l_0)^4}{l_0 l_2^3(3l_1l_0 + 3l_2l_0 + 2l_1l_2 + 3l_0^2)(l_1^2 + l_1l_2 + l_1l_0 + l_2^2 + l_2l_0)} \tag{21}$$

In order to find the ratio of link lengths which maximizes X^* or minimizes λ^*, we first normalize lengths by setting $l_0 = 1$, and denote the total swimmer's length by $l = l_0 + l_1 + l_2$. Figure 6 plots the optimal tail-to-head length ratio l_2/l_1 which maximizes X^* as a function of the total length l. It can be seen that the optimal ratio l_2/l_1 which maximizes X^* is less than unity, which implies that the tail should be shorter than the head. Moreover, it can be verified that for $l/l_0 \to \infty$, the optimal ratio converges to 1. On the other hand, for $l/l_0 < 4$ the optimal ratio which maximizes X^* is $l_2 \to 0$, meaning that the tail should be as short as possible. This result is a shortcoming of the simplified model, since a tail of vanishing length $l_2 \to 0$ with a torsional spring that applies torque according to $\tau_2 = -k\phi_2$ requires that the fluid generates an *external torque* concentrated at the swimmer's endpoint, which is unphysical[1]. A very interesting result is that the optimal ratio l_2/l_1 required to minimize the work-per-distance λ^* is precisely *the inverse* of the optimal ratio l_2/l_1 required to maximize the net travel distance X^*, as shown in Figure 6. That is, in order to minimize the energy expenditure per distance, the head should be shorter than the tail.

[1] It can also be shown that the maximal average velocity V^* and the maximal Lighthill efficiency η^* also attain their maximal value as the length of the tail vanishes $l_2 \to 0$.

Mathematically, this is a consequence of the fact that the inverse of the expression for X^* in (21) is proportional to the expression for λ^* when the lengths l_1 and l_2 are interchanged. Importantly, note that this key relation is not limited to the specific formulation of X^* and λ^* using the RFT approximation, but it is actually a fundamental property which is independent of the exact model used to explicitly formulate (2), (1) and (3). A detailed proof of the latter statement, which is based on geometric symmetries of the swimmer's equation of motion, can be found in [33].

5 Conclusion

The dynamics of Purcell's three-link swimmer with a passive elastic tail has been analyzed. Leading-order expressions for the swimmer's motion and energy expenditure were formulated by using perturbation expansion about the actuation amplitude. The dependence of the motion on the actuation amplitude ε and frequency ω has been elucidated. It was found that there exist intermediate frequencies ω_c and ω_η which, to leading order in ε, maximize the net forward motion per period X and the Lighthill efficiency η, respectively. It was also found that the average velocity V is maximized for $\omega \to \infty$ and the average mechanical work per forward distance λ is minimized for $\omega \to 0$, both converging to finite nonzero limits. Using the RFT formulation, optimization of the link lengths has been conducted. It was found that X is maximized by taking a tail which is shorter than the head, and that precisely the inverse ratio is required in order to minimize λ. For cases where the length l_0 of the middle link ("body") is significant, the optimization results are unphysical and reflect the shortcoming of this oversimplified model, in which the elasticity of the entire swimmer is concentrated at a single point.

Some possible directions for future extensions of the research are briefly listed as follows. First, higher order terms in the expansion are currently under systematic computation, and their incorporation appears to greatly improve the accuracy of the theoretical predictions. Second, nonzero-mean actuation should be considered, in order to account for steering capabilities of the swimmer. Third, a more physically realistic model should be considered, where the elasticity is distributed along the filament. This can be modeled either as a multiple degrees-of-freedom system, or a partial differential elasticity equation in the spirit of [24–26]. Additionally, the leading-order contribution of inertial effects at high actuation frequencies (large Strouhal number) should be considered. Finally, a robotic three-link swimmer prototype has been recently designed and constructed [Fig. 7], and preliminary motion experiments are currently being conducted in order to demonstrate the theoretical predictions.

YO wishes to thank Gilead Tadmor for fruitful discussions which have initiated this study. We thank the anonymous reviewer for useful comments which helped improving the quality of this paper.

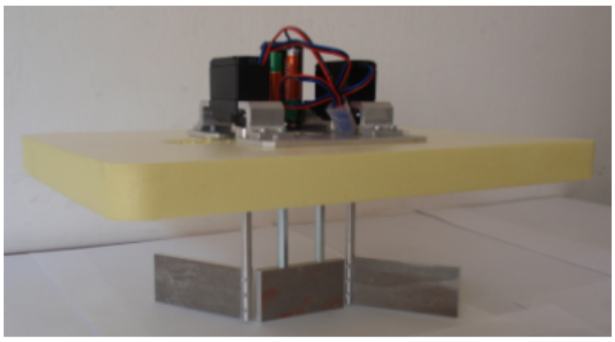

Fig. 7. Robotic prototype of the three-link swimmer.

References

1. Brennen and H. Winet. Fluid mechanics of propulsion by cilia and flagella. *Annu. Rev. Fluid Mech.*, 9:339–398, 1977.
2. J. Happel and H. Brenner. *Low Reynolds Number Hydrodynamics*. Prentice-Hall, 1965.
3. E. Lauga and T. R. Powers. The hydrodynamics of swimming microorganisms. *Rep. Prog. Phys.*, 72:096601, 2009.
4. E. M. Purcell. Life at low Reynolds number. *Am. J. Phys.*, 45:3–11, 1977.
5. J. Gray and H. W. Lissmann. The locomotion of nematodes. *J. Exp. Biol.*, 41:135–154, 1964.
6. K. E. Machin. Wave propagation along flagella. *J. Exp. Biol*, 35:796–806, 1958.
7. C. J. Brokaw. Flagellar movement: A sliding filament model. *Science*, 178:455–462, 1972.
8. S. Camalet, F. Jülicher, and J. Prost. Self-organized beating and swimming of internally driven filaments. *Physical Review Letters*, 82(7):1590–1593, 199.
9. E. A. Gaffney, H. Gadelha, D. J. Smith, J. R. Blake, and J. C. Kirkman-Brown. Mammalian sperm motility: Observation and theory. *Annu. Rev. Fluid Mech.*, 43:501–528, 2011.
10. R. Dreyfus, J. Baudry, M. l. Roper, M. Fermigier, H. A. Stone, and J. Bibette. Microscopic artificial swimmers. *Nature*, 437:862–865, 2005.
11. B. J. Nelson, I. K. Kaliakatsos, and J. J. Abbott. Microrobots for minimally invasive medicine. *Review of Biomedical Engineering*, 12:55–85, 2010.
12. G. I. Taylor. Analysis of the swimming of microscopic organisms. *Proc. Roy. Soc. A*, 209:447–461, 1951.
13. J. Gray and G. J. Hancock. The propulsion of sea-urchin spermatozoa. *J. Exp. Biol.*, 32:802–814, 1955.
14. M. J. Lighthill. On the squirming motion of nearly spherical deformable bodies through liquids at very small Reynolds numbers. *Comm. Pure Appl. Math.*, 5:109–118, 1952.
15. J. R. Blake. A spherical envelope approach to ciliary propulsion. *J. Fluid Mech.*, 46:199–208, 1971.
16. A. Najafi and R. Golestanian. Simple swimmer at low Reynolds numbers: Three linked spheres. *Phys. Rev. E*, 69:062901–062904, 2004.
17. J. E. Avron, O. Kenneth, and D. H. Oakmin. Pushmepullyou: An efficient micro-swimmer. *New J. Phys.*, 7:234238, 2005.
18. A. M. Leshansky and O. Kenneth. Surface tank treading: Propulsion of Purcell's toroidal swimmer. *Phys. Fluids*, 20:063104, 2008.

19. L. E. Becker, S. A. Koehler, and H. A. Stone. On self-propulsion of micro-machines at low Reynolds numbers: Purcell's three-link swimmer. *J. Fluid Mech.*, 490:15–35, 2003.
20. R. G. Cox. The motion of long slender bodies in a viscous fluid part 1. general theory. *J. Fluid Mech.*, 44:791–810, 1970.
21. D. Tam and A. E. Hosoi. Optimal stroke patterns for Purcell's three-link swimmer. *Phys Rev. Lett.*, 98:068105, 2007.
22. J. E. Avron and O. Raz. A geometric theory of swimming: Purcell's swimmer and its symmetrized cousin. *New J. Phys.*, 10:063016, 2008.
23. Y. Or. Asymmetry and stability of shape kinematics in microswimmers' motion. *Phys Rev. Lett.*, 108:258101, 2012.
24. C. H.Wiggins and R. E. Goldstein. Flexive and propulsive dynamics of elastica at low Reynolds number. *Physical Review Letters*, 80:3879–3882, 1998.
25. M. L. Roper, R. Dreyfus, J. Baudry, M. Fermigier, J. Bibette, and H. A. Stone. On the dynamics of elastic driven filaments. *J. Fluid Mech.*, 554:167–190, 2006.
26. E. Lauga. Floppy swimming: Viscous locomotion of actuated elastica. *Physical Review E*, 75:041916, 2007.
27. A. Shapere and F. Wilczek. Geometry of self-propulsion at low Reynolds numbers. *J. Fluid Mech.*, 198:557–585, 1989.
28. A. H. Nayfeh. *Perturbation methods*. Willey-VCH, 2004.
29. J. Lighthill. *Mathematical Biofluiddynamics*. SIAM, Philadelphia, PA, 1975.
30. E. M. Purcell. The efficiency of propulsion by a rotating flagellum. *Proc. Natl Acad. Sci.*, 94:11307–11311, 1997.
31. J. E. Avron, O. Gat, and O. Kenneth. Optimal swimming at low Reynolds numbers. *Phys Rev. Lett.*, 93(18):186001, 2004.
32. S. Childress. A thermodynamic efficiency for Stokesian swimming. *J. Fluid Mech.*, 2012 (online), DOI: 10.1017/jfm.2011.561.
33. A supplementary document *supp1.pdf* with more technical details is submitted online along with the manuscript.